Grain boundary segregation of alloying Cu induced intergranular corrosion of B$_4$C-6061Al composite

Y.T. Zhou [a,*], Y.N. Zan [b], Q.Z. Wang [b], B.L. Xiao [c], Z.Y. Ma [c], X.L. Ma [a]

[a] *Shenyang National Laboratory for Materials Science, Institute of Metal Research, Chinese Academy of Sciences, 72 Wenhua Road, Shenyang 110016, China*
[b] *CAS Key Laboratory of Nuclear Materials and Safety Assessment, Institute of Metal Research, Chinese Academy of Sciences, 72 Wenhua Road, Shenyang 110016, China*
[c] *Shi-changxu Innovation Center for Advanced Materials, Institute of Metal Research, Chinese Academy of Science, 72 Wenhua Road, Shenyang 110016, China*

A B S T R A C T

The intergranular corrosion (IGC) and the microstructures in B$_4$C-reinforced 6061Al composite were investigated in the present work. IGC only occurred in the Cu-containing samples. The artificial aging decreased the IGC resistance of the composite. Corrosion propagated through the aluminum grain boundaries as well as the B$_4$C/Al interfaces. The microstructures characterizations by transmission electron microscopy (TEM) indicated that a continuous Cu-rich layer with width of 3.5 nm along grain boundary was responsible for the IGC susceptibility of aged Cu-containing sample.

1. Introduction

B$_4$C particles-reinforced Al-matrix (B$_4$C—Al) composites have been increasingly used as a neutron absorber material in the nuclear industry owing to the high strength, light weight, and particularly the neutron absorbing property [1–3]. For commercial application, Al-Mg-Si (6xxx series) alloys are often used as the composite matrix when the mechanical property is required. Since the composites are served in aqueous environment when the spent nuclear fuel is wet-stored, the corrosion resistance of the composites should be seriously considered [4–8]. The previous research works have shown that B$_4$C-Al composites were susceptive to pitting corrosion in Cl$^-$- containing solution [9,10]. The B$_4$C particles as well as other secondary phases, *e.g.* Mg(Al)B$_2$ are the sites where pits preferred to initiate [7–10].

Intergranular corrosion (IGC) is frequently observed on Cu-containing Al-Mg-Si alloys [11]. IGC is a dangerous corrosion form since it propagates inwards and weakens the grain bonding. The IGC susceptibility of the alloys is closely related to the compositions *i.e.*, Si: Mg ratio and particularly, Cu content [12–15]. Cu content as low as 0.1 wt% can cause Q-phase precipitation along grain boundaries [16]. According to the electrochemical microcell and quasi *in-situ* transmission electron microscopy (TEM) studies, Q-phase was found to be cathodic with respect to pure Al and θ-phase [17]. The potential gaps among the aluminum matrix, grain boundary precipitates and the precipitate-free

zones (PFZs) were demonstrated to be the reasons for IGC [14,18,19]. Therefore, the IGC susceptibility is controlled by artificial aging conditions as well. Under aged Cu-containing alloys are prone to IGC. IGC depths were increased up to the peak aged condition and then decreased in the over aged condition [20]. Overaging was demonstrated to reduce the electrochemical potential difference between the matrix and the depleted zone due to the extensive precipitation in the matrix [21]. The other mechanism for Cu-induced IGC was attributed to the continuous copper-rich film along the grain boundaries. Such film was observed in under aged alloys by different authors [15,20,22,23]. In over aged tempers, however, the growth of discrete precipitates consumed Cu and thereby disrupted the continuity of the Cu film. This also explained the decrease of IGC susceptibility of over aged alloys.

In terms of the B$_4$C-reinforced Al-Mg-Si (—Cu) composites, the Cu distribution is much distinct with that in alloys. As we mentioned in a recent work [24], the interfacial chemical reactions between B$_4$C and the alloy matrix generated abundant magnesium boride compounds and resulted in the depletion of element Mg in the matrix. Cu did not form precipitates but segregated along interphase boundaries. Consequently, the corrosion mechanism in the composite is different in comparison to Al-Mg-Si-Cu alloys [25]. It has been reported that the Mg/Cu co-segregation along interphase boundaries underwent preferential dissolution prior to the local stable pitting occurrence. The Cu-rich remnant and Mg(Al)B$_2$ dispersoids then played a cathodic role, accelerating

dissolution of the surrounding Al-matrix. To date, it is still unclear whether Cu addition will influence the IGC resistance of the composite, and what the mechanism is? In consideration of the application safety, the problems should be ascertained. In the present work, IGC of the B_4C-reinforced Al-Mg-Si-Cu composite was studied. The microstructural mechanisms for IGC were analyzed by advanced electron microscopy techniques.

2. Material and methods

The composite was fabricated by powder metallurgy technique. The nominal composition of the alloy matrix was Al-1.0Mg-0.65Si-0.25Cu (wt%) (6061Al). The mean sizes of the alloy and B_4C powders were 13 and 7 µm, respectively. As a comparison, the alloy matrix without Cu was also prepared. The two samples were named after 0.25Cu and 0Cu, respectively, for short. The as-mixed alloy and B_4C powders (21 wt%) were cold pressed in a cylindrical die under a pressure of 50 MPa and then hot pressed at 620 °C under a pressure of 30 MPa for 2 h, producing the composite billets. The billets were then hot forged at 450 °C. The forged samples were solution treated at 530 °C for 2.5 h, water quenched. A part of the 0.25Cu samples were aged at 175 °C for 6 h (T6 treatment for 6061Al) and named as 0.25Cu-A.

Electrochemical tests (potentiodynamic polarization measurements) were carried out on an AUTOLAB PGSTAT302N electrochemical workstation. A traditional three-electrode system, *i.e.* the composite sample as the working electrode, a platinum foil as the counter electrode and a saturated calomel electrode (SCE) as the reference electrode, was used. The tested samples were cut into 1 cm × 1 cm slices, then ground to 2000 grit *SiC* papers and polished by diamond paste to 5 µm finish. Potentiodynamic scan was started at 250 mV below VOC and at a rate of 0.33 mV/s in 0.1 M NaCl solution at room temperature. Three specimens per condition were measured to ensure the accuracy of tests.

ASTM G110 was referred for the IGC tests [26]. Samples for the IGC testing were ground to 2000 grit *SiC*. Specimens were immersed in etching solution, 50 mL HNO_3 (70%) + 950 mL deionised water at 93 °C for 1 min and rinsed in deionised water. Then the specimens were further immersed in concentrated HNO_3 (70%) at room temperature for 1 min and rinsed in deionised water and air dried. Following these pretreatment steps, specimens were finally experienced IGC test in 1 L NaCl (1 mol/L) + 10 mL H_2O_2 (30%) solution at room temperature for 6 h. The tested specimens were taken out and cleaned by deionised water and air dried. The surface corrosion products were not removed. For SEM characterization, the dried specimens were cut, cold mounted with the exposure of cross sections. The mounted specimens were ground to 1 µm diamond finish.

The IGC tested samples were characterized by Hitachi SU-70 scanning electron microscope (SEM). Low magnification TEM characterizations were performed using FEI Tecnai G^2 F30 microscope equipped with high-angle annular dark-field (HAADF) and EDS detectors. The atomic-scale TEM experiments were conducted by an FEI Titan G^2 60–300 aberration-corrected TEM. The HAADF image provides the Z-contrast which is proportional to the local compositions and the specimen thickness [27]. TEM specimens were prepared by a regular method, *i.e.* mechanical polishing and ion-milling using Gatan PIPS 691.

3. Results

The potentiodynamic polarization curves of the samples 0Cu, 0.25Cu and 0.25Cu-A are shown in Fig. 1. From the anodic branches of all the polarization curves, steep rises in the current to near 10 mA/cm^2 were observed at the corrosion potential (E_{corr}). The breakdown occurred at the potential suggested that all the samples were vulnerable to the chloride ions owing to the discontinuity of the protective surface oxide films. The difference in corrosion resistance of the samples could be evaluated by their corrosion current density (i_{corr}) derived from the curves [9]. It is obvious that the i_{corr} of the sample 0Cu ($\sim$2.4 µA/cm^2)
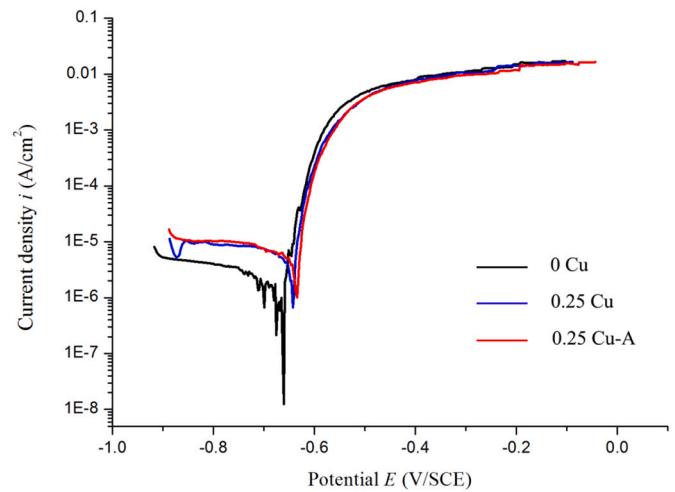

Fig. 1. Potentiodynamic polarization curves of the samples 0Cu (black), 0.25Cu (blue), and 0.25Cu-A (red) in 0.1 M NaCl solution at room temperature. (For interpretation of the references to colour in this figure legend, the reader is referred to the web version of this article.)

was smaller than the Cu-containing samples, while the latter two did not show much different ($\sim$6.5 µA/cm^2 and $\sim$7.3 µA/cm^2 for 0.25Cu and 0.25Cu-A, respectively).

The IGC resistance of the composites was compared by immersion tests. Cross-sectional micrographs of the specimens 0Cu, 0.25Cu and 0.25Cu-A after IGC tests are shown in Fig. 2(a)–(c), respectively. The top-most white layer in the secondary-electron images are corrosion products on the samples surfaces. The corroded 0Cu sample exhibited typical pitting morphology (Fig. 2(a)). Careful examining all the corroded 0Cu samples indicated that the grain boundaries were not attacked. Fig. 2(b) shows the corroded 0.25Cu sample, exhibiting the pitting characteristic and localized IGC. The zoom-in image of the corroded area is given in the inset. The corrosion fissure was observed at the bottom of the pit. In contrast, a widely expanded fissure network was observed over the entire surface of the aged specimen 0.25Cu-A in Fig. 2 (c), indicating the sample was IGC prone. The IGC depth was larger than 150 µm beneath the corrosion products layer. The thicker corrosion product layer on the sample 0.25Cu-A also suggested more severe attack in this specimen. The IGC front in the sample 0.25Cu-A was closely inspected to figure out the IGC propagating routes. Fig. 2(d) shows that the B_4C/Al interfaces as marked by the blue arrows, besides the grain boundaries, played an important role for IGC development. IGC along the B_4C/Al interface then branched out when it met grain boundaries. Moreover, several sites as denoted by yellow arrows were etched, leaving small undissolved particles inside. EDS analysis revealed the particles were a ternary phase containing Mg, Al and B.

To explore the microstructural causes of IGC in the composite, TEM analysis was performed comparatively on the above three samples. The main attention in this work was paid to the grain boundaries. Fig. 3(a) and (b) show the HAADF-STEM images of the alloy matrices in the samples 0Cu and 0.25Cu. Based on the low-magnification micrographs, no apparent difference in the two samples could be found. The grain boundaries were depicted by yellow dot lines. Two types (denoted as Type A and Type B in the figures) of nano-sized dispersoids were observed at grain boundaries and in the grain interior. The Type A was always found in the form of aggregate. The size of a single particle was in the range of 10–20 nm. The other type had lower contrast and was about several tens of nm in diameter (a few of the dispersoids were larger than 100 nm). By electron diffraction and EDS analysis, the two kinds of dispersoids were identified.

Fig. 4(a) is a bright-field (BF) micrograph of the Type A dispersoids at a grain boundary. EDS mapping in Fig. 4(b) shows that these nano-
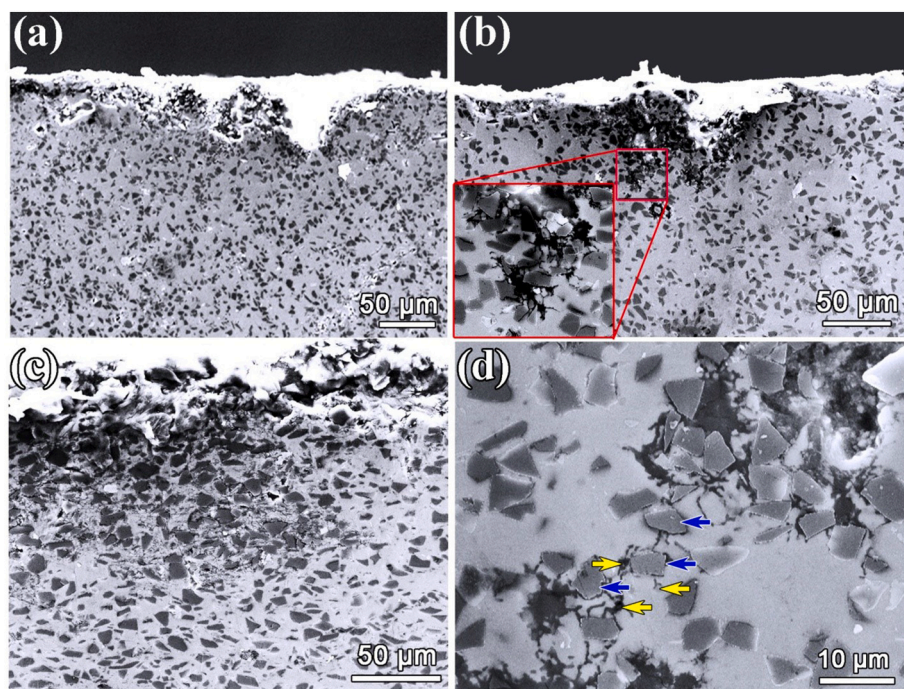
Fig. 2. Representative cross sectional corrosion morphologies following 6 h exposure in test solution. (a) pitting corrosion (sample 0Cu), (b) pitting corrosion and localized IGC (sample 0.25Cu), (c) typical IGC (sample 0.25Cu-A), (d) zoom-in image of the IGC front in the sample 0.25Cu-A, the corrosion expansion along the B_4C/Al interfaces and the small particles inside the corrosion areas were denoted by blue and yellow arrows, respectively. (For interpretation of the references to colour in this figure legend, the reader is referred to the web version of this article.)
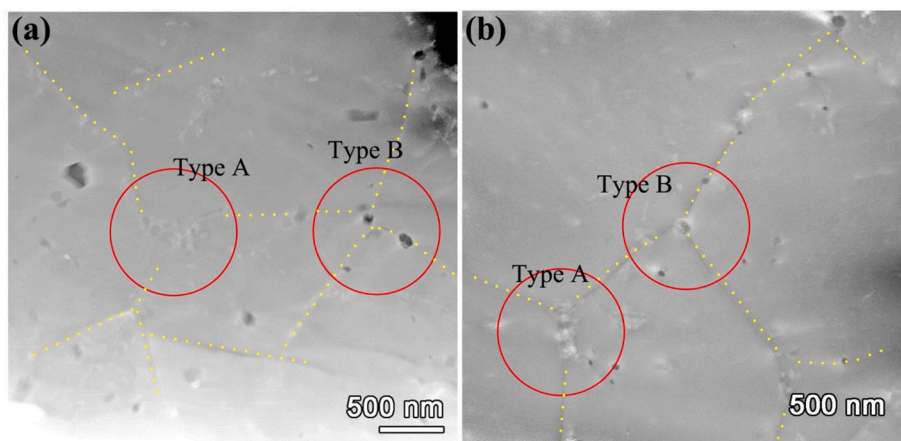

Fig. 3. STEM images of the aluminum matrix in (a) the sample 0Cu, (b) the sample 0.25Cu. The grain boundaries were depicted by dot lines. Two types (Type A and Type B in the figures) of nano-sized dispersoids were observed.

particles are composed of Mg, Al and O. Electron diffraction of the particle denoted by a red circle in Fig. 4(a), combining with the compositional information, revealed that the particle was a $MgAl_2O_4$ spinel with lattice constant of $a = 0.81$ nm. The $MgAl_2O_4$ particles were introduced from the surface oxide film on alloy powders.

Fig. 5 is a BF-TEM image and corresponding electron diffraction pattern of the Type B particle located at a grain boundary junction. It indicated that the particle was a $Mg(Al)B_2$ nano-crystal which has been characterized in detail in our previous work [10]. The nano-crystal has a rod-shape and the axial direction is along the [0001] zone-axis. They are the products of the chemical reactions between B_4C and the alloy matrix *via* the routes [24]:

$$3Al + B_4C \rightarrow Al_3BC + 3B; \; ② \; 2B + Mg(Al) \rightarrow Mg(Al)B_2 \quad (1)$$
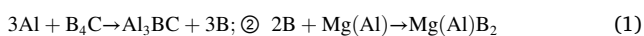
Reaction (1) generates Al_3BC compound and free boron. The Al_3BC compounds were always found at the B_4C/Al interfaces. Characterizations on the Al_3BC layer will be shown in the following. Free boron diffuses into the partially melted alloy matrix, yielding $Mg(Al)B_2$

dispersoids. During the hot-deformation process, the dispersive $Mg(Al)B_2$ particles impede the grain boundary migration and consequently, are frequently seen at the boundaries and grain triple junctions.

Extensive TEM experiments did not reveal other secondary phases along grain boundaries in the two samples. Since the above two dispersoids are very thermally stable, their types and amounts did not change when the 0.25Cu sample was artificially aged.

After then, high-resolution TEM characterizations were conducted on the grain boundaries in these samples. Fig. 6(a) shows a low-magnification STEM image of the boundaries pinned by $Mg(Al)B_2$ dispersoids in the sample 0.25Cu-A. Zoom-in on the grain boundary area as framed in Fig. 6(a), we could not find any discrete precipitate at the boundaries and in the grain interior (Fig. 6(b)). A tilting examination was also performed, suggesting the grain boundary was actually precipitate-free (Fig. 6(c)). However, EDS mapping as shown in Fig. 6 (d)–(g) clearly exhibited the Cu enrichment along the $Mg(Al)B_2$/Al interface as well as the grain boundary.

To obtain the atomic-scale structural information, the boundary was
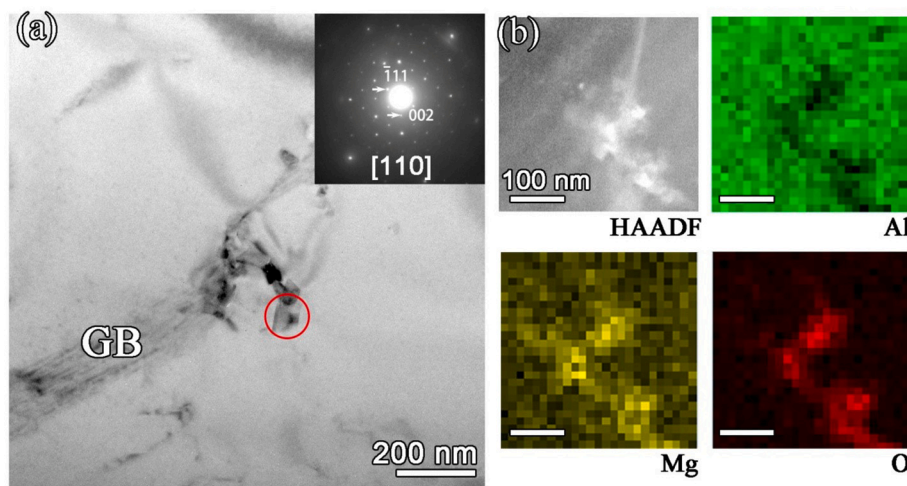
Fig. 4. Characterizations of the oxide nanoparticles. (a) Bright-filed (BF) TEM image of the particles located at a grain boundary (GB) in the sample 0.25Cu. The selected-area electron diffraction (SAED) pattern was obtained from the particle denoted by the red circle. (b) EDS mapping of the nano-particles indicated they were composed of Mg, Al and O. These particles could be identified as $MgAl_2O_4$ by the diffraction and EDS information. Bar = 100 nm. (For interpretation of the references to colour in this figure legend, the reader is referred to the web version of this article.)
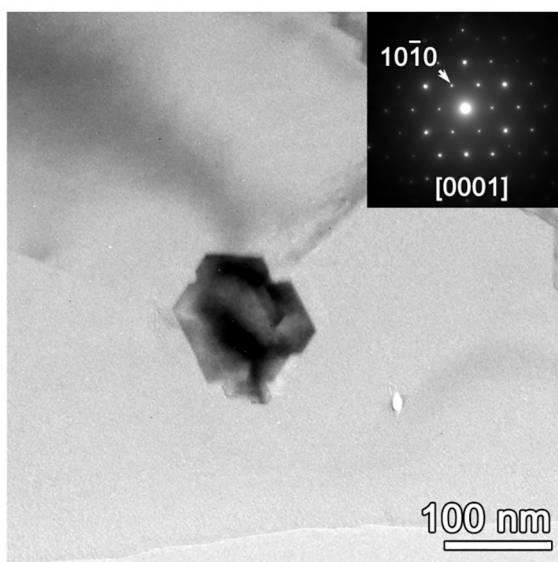

Fig. 5. BF TEM image and the corresponding SAED pattern of a $Mg(Al)B_2$ particle in the alloy matrix in the sample 0Cu.

then characterized by aberration-corrected STEM (Fig. 7(a)). It was hard to ensure that the grains on the two sides were exactly oriented along the low index zone-axis and showed their lattices by tilting the TEM foil. The enlarged image of the grain boundary is displayed in Fig. 7(b). The grain on the right hand in Fig. 7(a) was viewed along the [001] zone-axis which usually is the proper direction to characterize Q phase [28]. Seen from the crystalline lattice in the STEM images, there was no well-defined precipitate, but a continuous Cu-rich layer along the boundary. The contrast profile measured across the boundary (as denoted by the red rectangle in Fig. 7(b)) suggested the Cu-rich layer being about 3.5 nm in width.

As a comparison, the characterization results of the grain boundary in the sample 0.25Cu are presented in Fig. 8. It was seen that the $Mg(Al)B_2/Al$ interfaces were also rich in Cu solute. However, no obvious Cu signal could be detected along the grain boundary.

Since the B_4C/Al interface is an important propagating route for IGC, the interphase boundary in the Cu-containing composite was studied by TEM as well. Fig. 9(a) shows the interface between a B_4C particle and the alloy matrix. A thin layer which consisted of randomly oriented Al_3BC particles was observed at the interface (denoted by dot lines). SAED pattern of an individual Al_3BC particle is shown in Fig. 9(b). The results of EDS mapping performed on an Al_3BC particle when it was tilted along the $\left[1\bar{2}10\right]$ zone axis are displayed in Fig. 9(c)–(g). The Cu-enrichment around the Al_3BC particle was evidently seen.

4. Discussion

The electrochemical polarization measurements indicated that the Cu-containing B_4C-6061Al composites had worse corrosion resistance than the Cu-free sample. The sample 0Cu showed relatively lower cathodic current density and corrosion current density (i_{corr}), while the polarization curves of 0.25Cu and 0.25Cu-A were almost the same. The micro-galvanic couples in these composites include the $B_4C/Al_3BC/Al$ system and $Mg(Al)B_2/Al$ system. The only difference existed between Cu-containing and Cu-free samples, to our knowledge, mainly is the Cu/Mg-rich layer surrounding $Mg(Al)B_2$ and Al_3BC particles in both 0.25Cu and 0.25Cu-A samples. The cathodic effect of the layers [25] should be responsible to the higher cathodic dynamics in the Cu-containing samples. The selective dissolution of Mg from this layer is similar to Q-phase and S-phase, which resulted in cathodic Cu residues [17,26,29]. From the polarization results, we could not find apparent difference between the samples 0.25Cu and 0.25Cu-A. In fact, the microstructures in these two samples are very identical. Due to the consumption of alloying element Mg, artificial aging actually did not generate any precipitate in the grain interior and at grain boundaries, which is also supported by the negligible aging-hardening ability of the composite [30]. Only when the grain boundary was examined at an atomic level, we could found that the Cu solute diffused and segregated along grain boundaries during aging. The microstructural characteristics in the 0.25Cu-A is believed not to give rise to much difference in the polarization curves. However, the present research clearly demonstrated that the Cu-enriched film along the grain boundaries could dominantly cause IGC susceptibility of the B_4C-6061Al composite.

In 6xxx series Al-alloys , such kind of 'wetting Cu layer' along grain boundaries were always found to co-exist with Q-phases. Generally speaking, metallic copper and Cu-containing precipitates possess more noble corrosion potentials than pure aluminum. It was conceived that the continuous Cu layer at the GBs acted as cathode and resulted in the accelerated dissolution of the adjacent solute-depleted zone [22]. By means of STEM and 3D atom probe tomography (APT), the presence of discrete Q-phase precipitates and an ultra-thin Cu layer along grain boundaries were confirmed by Larsen et al. [23] and Kairy et al. [20,31]. Moreover, a solute-depleted zone adjacent to the grain boundaries was also detected. In the present observations, IGC took place in the Cu-containing samples and became severe in the aged sample. By careful
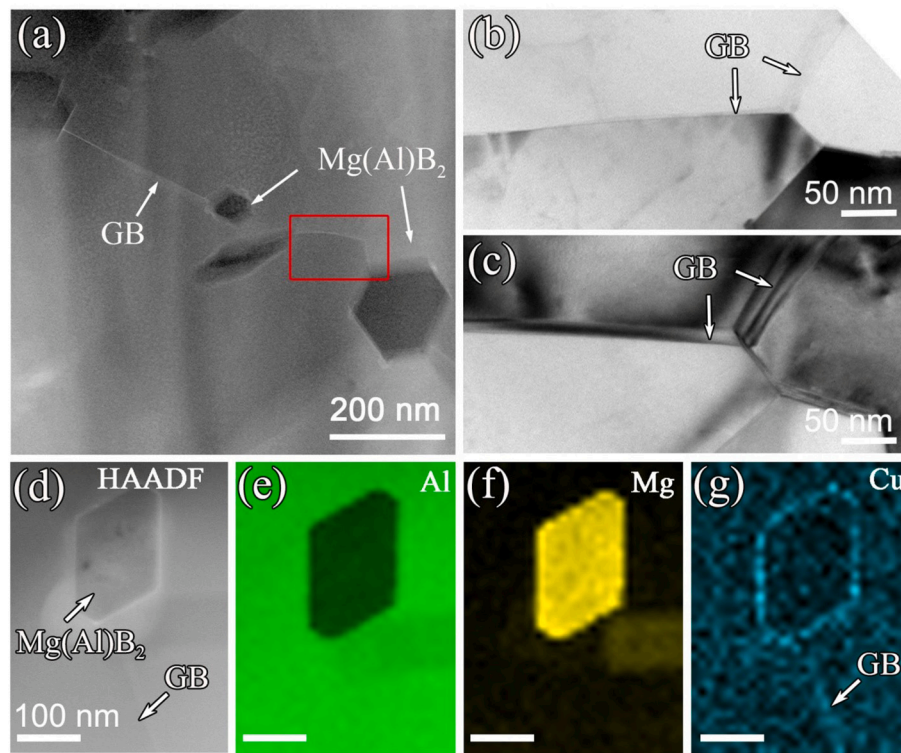
Fig. 6. (a) STEM image of the grain boundary pinned by Mg(Al)B$_2$ dispersoids in the sample 0.25Cu-A. The bright contrast of grain boundaries (GBs) indicates the heavy elements enrichment. (b) and (c) BF TEM image and a tilted view of the grain boundary framed in (a), showing no discrete precipitate at the boundary. (d)-(g) EDS elemental mapping showing the Cu segregation surrounding the Mg(Al)B$_2$ nano-particle and along the grain boundary as well. Bar = 100 nm.
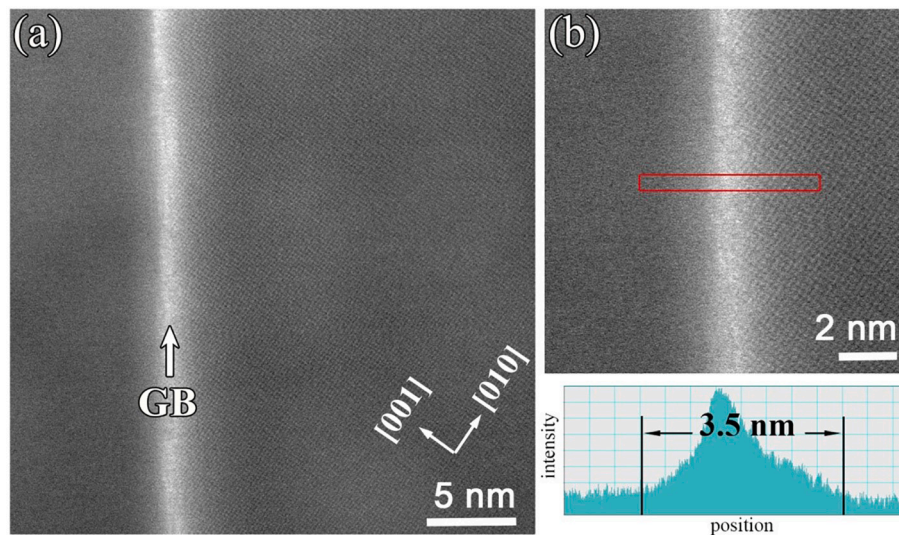

Fig. 7. (a) High resolution STEM image of a part of the grain boundary. (b) An enlarged part of the STEM image in (a). The bright contrast along the boundary shows the continuous Cu-rich layer. The width was measured to be about 3.5 nm according to the contrast profile.

TEM examinations, we found only the continuous Cu film but no precipitate along the grain boundaries in the B$_4$C-6061Al composite. Such Cu-rich boundaries were more frequently seen in the sample 0.25Cu-A, compared with the solution treated samples 0.25Cu (Figs. 6 and 7). The IGC tests strongly suggest that the Cu wetting layer alone could result in the IGC susceptibility of the composites. On the other hand, as reported in Ref. [23,31], the authors found a Cu/Si-depleted zone on both sides of a grain boundary. Due to the sensitivity limits of the EDS technique and the low Cu level in the alloy matrix, we could not detect the solute depletion adjacent to grain boundaries.

Based on the SEM observations in Fig. 2(d), the microstructures and IGC characteristics are schematically summarized in Fig. 10. Besides the grain boundaries, B$_4$C/Al interfaces are the significant routes for IGC propagation as well. As shown in Fig. 9, the B$_4$C/Al interface is actually a multi-phase system. The electrochemical effect of each component could not be easily excluded. Firstly, B$_4$C possesses a noble electrode potential relative to the aluminum matrix [32,33]. Although the galvanic current in the B$_4$C/Al system is quite low [34], the galvanic cell probably exists between B$_4$C particles and the matrix. In addition, the semiconductor Al$_3$BC layer at the B$_4$C/Al interface increases the complexity of the
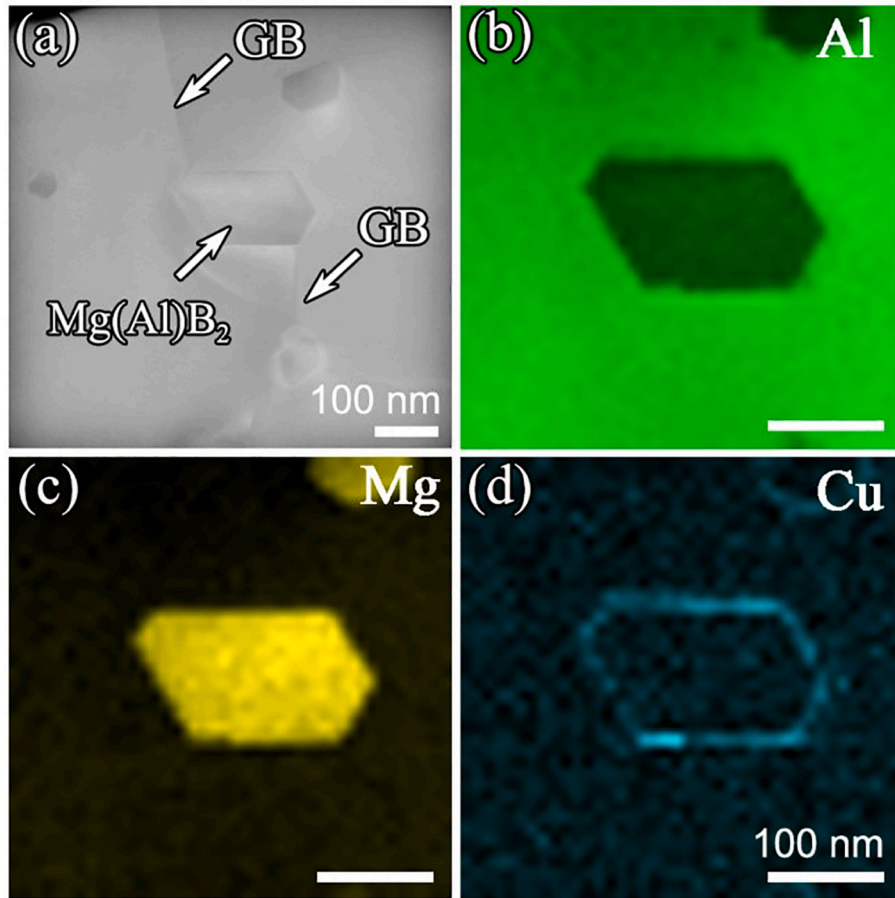
Fig. 8. (a) STEM image of the $Mg(Al)B_2$ dispersoids and the grain boundary in the sample 0.25Cu. (b)–(d) EDS elemental mapping of the $Mg(Al)B_2$ particle at the center part of (a). The Cu segregation is only found at the $Mg(Al)B_2/Al$ interfaces. Bar = 100 nm.
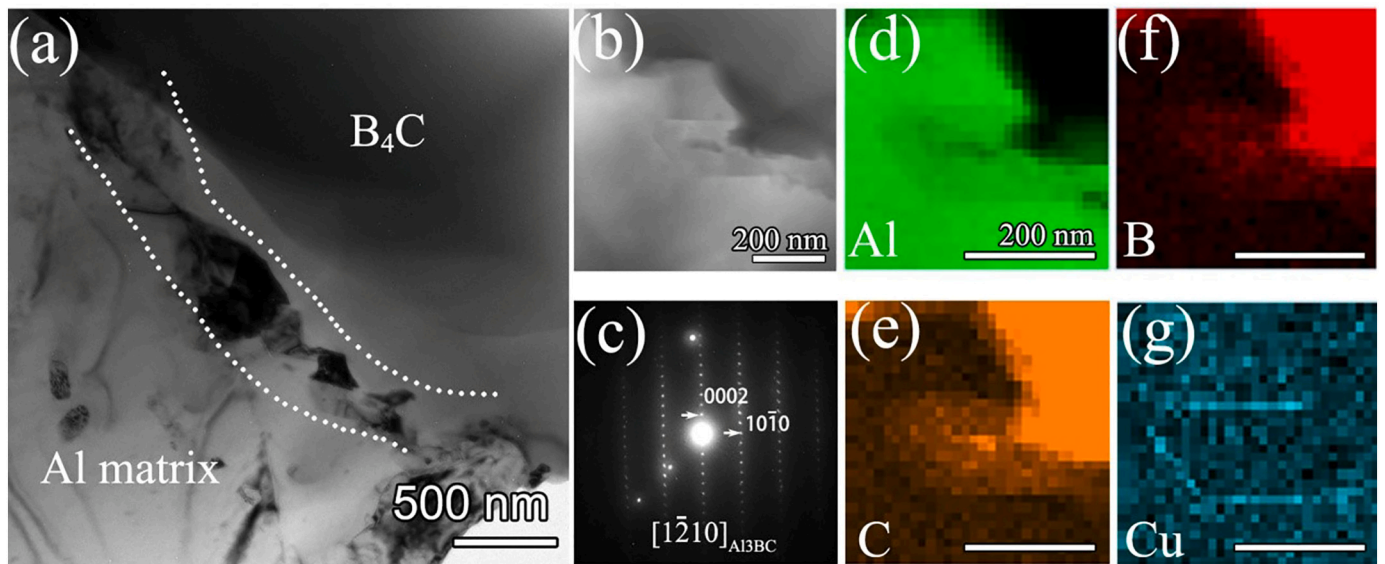

Fig. 9. Characterizations of the B_4C/Al interface in the sample 0.25Cu-A. (a) BF TEM image of the B_4C/Al interface where an Al_3BC layer (denoted by dot lines) is located at the interface. (b) HAADF image of the B_4C/Al interface when a single Al_3BC particle was tilted along its $\left[1\bar{2}10\right]$ zone axis. (c) SAED pattern of the Al_3BC particle in (b). (d)–(g) EDS mapping showing the Cu segregation around the Al_3BC particle. Bar = 200 nm.
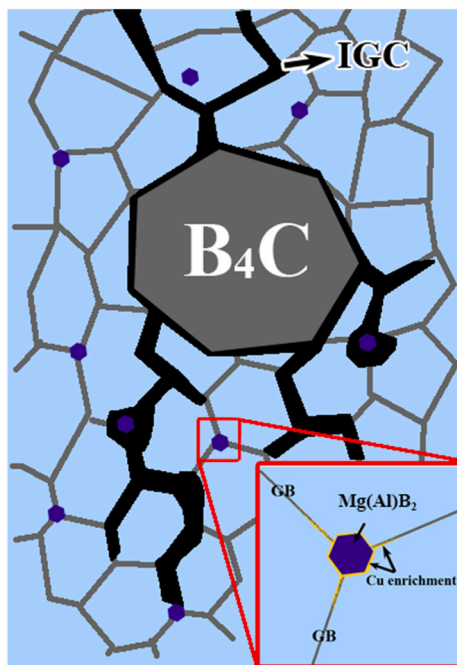
Fig. 10. Schematic of the microstructures and IGC routes in the sample 0.25Cu-A.

galvanic system. The electrochemical role of Al_3BC is still unclear, but there is no evidence showing the strongly galvanic corrosion induced by the compound [10]. The third part is the Cu segregation around the Al_3BC particles. It could also play the same role as that at grain boundaries and induce the localized corrosion.

5. Conclusions

The IGC susceptibility of the B_4C particles-reinforced Al-Mg-Si (—Cu) composites was studied. Compared with the Cu-containing composite, the 0Cu sample exhibited lower corrosion current density. Artificial aging did not result in obvious change of potentiodynamic polarization behaviors of the Cu-containing composite, but increased the IGC susceptibility. The aluminum grain boundaries as well as the B_4C/Al interfaces provided the routes for corrosion propagation inwards. High resolution STEM characterization indicated that the continuous Cu-layer along grain boundaries was the main reason for IGC. Besides, the B_4C/Al galvanic cell and the Cu segregation surrounding the Al_3BC layers could contribute to the corrosion expansion along the B_4C/Al boundaries.

Data availability

The raw/processed data required to reproduce these findings cannot be shared at this time, as the data form part of another ongoing study.

Declaration of Competing Interest

The authors declare that they have no known competing financial interests or personal relationships that could have appeared to influence the work reported in this paper.

Acknowledgements

References

[1] X.-G. Chen, Application of Al-B_4C metal matrix composites in the nuclear industry for neutron absorber materials, in: N. Gupta, W.H. Hunt (Eds.), Solidification Processing of Metal Matrix Composites, TMS, USA, 2006, pp. 343–350.

[2] H.S. Chen, W.X. Wang, Y.L. Li, P. Zhang, H.H. Nie, Q.C. Wu, The design, microstructure and tensile properties of B_4C particulate reinforced 6061Al neutron absorber composites, J. Alloys Compd. 632 (2015) 23–29, https://doi.org/10.1016/j.jallcom.2015.01.048.

[3] Y.N. Zan, Q. Zhang, Y.T. Zhou, Q.Z. Wang, B.L. Xiao, Z.Y. Ma, Enhancing high-temperature strength of B_4C–6061Al neutron absorber material by in-situ Mg(Al) B_2, J. Nucl. Mater. 526 (2019) 151788, https://doi.org/10.1016/j.jnucmat.2019.151788.

[4] Y. Han, D. Gallant, X.-G. Chen, Galvanic corrosion associated with Al-B_4C composites/SS304 and Al-B_4C composites/AA6061 couples in NaCl and H_3BO_3 solutions, Electrochim. Acta 94 (2013) 134–142, https://doi.org/10.1016/j.electacta.2013.01.115.

[5] Y.M. Han, X.-G. Chen, Corrosion characteristics of Al-B_4C metal matrix composites in boric acid solution, Mater. Sci. Forum 877 (2016) 530–536.

[6] Q. Bai, L. Zhang, P. Zhu, Y. Ma, S. Xia, B. Zhou, The effect of surface chemical treatment on the corrosion behavior of an Al-B_4C metal matrix composite in boric acid solution at different temperatures, Corros. Sci. 164 (2020) 108356, https://doi.org/10.1016/j.corsci.2019.108356.

[7] Y.-L. Li, W.-X. Wang, H.-S. Chen, J. Zhou, Q.-C. Wu, Corrosion behavior of B_4C/6061Al neutron absorber composite in different H_3BO_3 concentration solutions, Acta Metal. Sin. (Engl. Lett.) 29 (2016) 1037–1046, https://doi.org/10.1007/s40195-016-0474-2.

[8] F. Zhang, J.B. Wierschke, X. Wang, L. Wang, Nanostructures formation in Al-B_4C neutron absorbing materials after accelerated irradiation and corrosion tests, Microsc. Microanal. 21 (Suppl. 3) (2015) 1159–1160, https://doi.org/10.1017/S1431927615006583.

[9] Y. Han, X.-G. Chen, Electrochemical behavior of Al-B_4C metal matrix composites in NaCl solution, Materials 8 (2015) 6455–6470, https://doi.org/10.3390/ma8095314.

[10] Y.T. Zhou, Y.N. Zan, X.X. Wei, B. Yang, B. Zhang, S.J. Zheng, X.H. Shao, J.H. Dong, X.L. Ma, B.L. Xiao, Q.Z. Wang, Z.Y. Ma, Corrosion onset associated with the reinforcement and secondary phases in B_4C-6061Al neutron absorber material in H_3BO_3 solution, Corros. Sci. 153 (2019) 74–84, https://doi.org/10.1016/j.corsci.2019.03.042.

[11] W.J. Poole, M.A. Wells, D.J. Lloyd, Investigation on microstructure and corrosion behaviour of 6XXX series aluminium alloys, Mater. Sci. Forum 519–521 (2006) 735–740, https://doi.org/10.4028/www.scientific.net/MSF.519-521.735.

[12] W.J. Liang, P.A. Rometsch, L.F. Cao, N. Birbilis, General aspects related to the corrosion of 6xxx series aluminium alloys: exploring the influence of Mg/Si ratio and Cu, Corros. Sci. 76 (2013) 119–128, https://doi.org/10.1016/j.corsci.2013.06.035.

[13] K. Shimizu, K. Nisancioglu, High resolution SEM investigation of intercrystalline corrosion on 6000-series aluminum alloy with low copper content, ECS Electrochem. Lett. 3 (2014) C29–C31, https://doi.org/10.1149/2.0041409eel.

[14] H. Zhan, J.M.C. Mol, F. Hannour, L. Zhuang, H. Terryn, J.H.W. de Wit, The influence of copper content onintergranular corrosion of model AlMgSi(Cu) alloys, Mater. Corros. 59 (2008) 670–675, https://doi.org/10.1002/maco.200804110.

[15] M.H. Larsen, J.C. Walmsley, O. Lunder, K. Nisancioglu, Effect of excess silicon and small copper content on intergranular corrosion of 6000-series aluminum alloys, J. Electrochem. Soc. 157 (2010) C61–C68, https://doi.org/10.1149/1.3261804.

[16] G. Svenningsen, J.E. Lein, A. Bjørgum, J.H. Nordlien, Y. Yu, K. Nisancioglu, Effect of low copper content and heat treatment on intergranular corrosion of model AlMgSi alloys, Corros. Sci. 48 (2006) 226–242, https://doi.org/10.1016/j.corsci.2004.11.025.

[17] S.K. Kairy, P.A. Rometsch, C.H.J. Davies, N. Birbilis, On the electrochemical and quasi in-situ corrosion response of the Q-phase ($Al_xCu_yMg_zSi_w$) intermetallic particle in 6xxx series Al-alloys, Corrosion 73 (2017) 87–99, https://doi.org/10.5006/2249.

[18] T. Minoda, H. Yoshida, Effect of grain boundary characteristics on intergranular corrosion resistance of 6061 aluminum alloy extrusion, Metall. Mater. Trans. A 33A (2002) 2891–2898, https://doi.org/10.1007/s11661-002-0274-3.

[19] C. Schnatterer, D. Zander, Influence of the grain boundary chemistry on the intergranular corrosion mechanisms of a high-strength Al-Mg-Si alloy, Surf. Interface Anal. (2015), https://doi.org/10.1002/sia.5859.

[20] S.K. Kairy, P.A. Rometsch, C.H.J. Davies, N. Birbilis, On the intergranular corrosion and hardness evolution of 6xxx series Al alloys as a function of Si:Mg ratio, Cu content, and aging condition, Corrosion 73 (2017) 1280–1295, https://doi.org/10.5006/2506.

[21] V. Guillaumin, G. Mankowski, Influence of overaging treatment on localized corrosion of Al 6056, Corrosion 56 (2000) 12–23, https://doi.org/10.5006/1.3280517.

[22] G. Svenningsen, M.H. Larsen, J.C. Walmsley, J.H. Nordlien, K. Nisancioglu, Effect of artificial aging on intergranular corrosion of extruded AlMgSi alloy with small Cu content, Corros. Sci. 48 (2006) 1528–1543, https://doi.org/10.1016/j.corsci.2005.05.045.

[23] M.H. Larsen, J.C. Walmsley, O. Lunder, R.H. Mathiesen, K. Nisancioglu, Intergranular corrosion of copper–containing AA6xxx AlMgSi aluminum alloys, J. Electrochem. Soc. 155 (2008) C550–C556, https://doi.org/10.1149/1.2976774.

[24] Y.T. Zhou, Y.N. Zan, S.J. Zheng, Q.Z. Wang, B.L. Xiao, X.L. Ma, Z.Y. Ma, Distribution of the microalloying element Cu in B_4C-reinforced 6061Al composites,

J. Alloys Compd. 728 (2017) 112–117, https://doi.org/10.1016/j.jallcom.2017.08.273.

[25] Y.T. Zhou, Y.N. Zan, Q.Z. Wang, B.L. Xiao, Z.Y. Ma, X.L. Ma, Atomic-scale quasi in-situ TEM observation on the redistribution of alloying element Cu in a B_4C/Al composite at the initial stage of corrosion, Corros. Sci. 174 (2020) 108808, https://doi.org/10.1016/j.corsci.2020.108808.

[26] ASTM G110, Standard Practice for Evaluating Intergranular Corrosion Resistance of Heat Treatable Aluminum Alloys by Immersion in Sodium Chloride + Hydrogen Peroxide Solution, ASTM International, West Conshohocken, PA, 2009.

[27] S.J. Pennycook, Structure determination through Z-contrast microscopy, Adv. Imag. Electron. Phys. 123 (2002) 173–206, https://doi.org/10.1016/S1076-5670(02)80063-5.

[28] H.S. Hasting, J.C. Walmsley, A.T.J. Van Helvoort, C.D. Marioara, S.J. Andersen, R. Holmestad, Z-contrast imaging of the arrangement of Cu in precipitates in 6XXX-series aluminium alloys, Philos. Mag. Lett. 86 (2006) 589–597, https://doi.org/10.1080/09500830600938340.

[29] R.G. Buchheit, M.A. Martinez, L.P. Montes, Evidence for Cu ion formation by dissolution and dealloying the Al_2CuMg intermetallic compound in rotating ring-disk collection experiments, J. Electrochem. Soc. 147 (2000) 119–124, https://doi.org/10.1149/1.1393164.

[30] Y.Z. Li, Q.Z. Wang, W.G. Wang, B.L. Xiao, Z.Y. Ma, Effect of interfacial reaction on age-hardening ability of B_4C/6061Al composites, Mater. Sci. Eng. A 620 (2015) 445–453, https://doi.org/10.1016/j.msea.2014.10.025.

[31] S.K. Kairy, T. Alam, P.A. Rometsch, C.H.J. Davies, R. Banerjee, N. Birbilis, Understanding the origins of intergranular corrosion in copper-containing Al-Mg-Si alloys, Metall. Mater. Trans. A 47A (2016) 985–989, https://doi.org/10.1007/s11661-015-3296-3.

[32] Y. Han, D. Gallant, X.-G. Chen, Investigation on corrosion behavior of the Al-B_4C metal matrix composite in a mildly oxidizing aqueous environment, Corrosion 67 (2011), https://doi.org/10.5006/1.3659505, 115005–1–115005-11.

[33] H. Ding, L.H. Hihara, Electrochemical examinations on the corrosion behavior of boron carbide reinforced aluminum-matrix composites, J. Electrochem. Soc. 158 (2011), https://doi.org/10.1149/1.3567519. C118–C124.

[34] H. Ding, L.H. Hihara, Electrochemical behavior of boron carbide and galvanic corrosion of boron carbide reinforced 6092 aluminum composites, ECS Trans. 1 (2006) 103–114, https://doi.org/10.1149/1.2215494.